materials

MDPI

Article

Carbonization and Preparation of Nitrogen-Doped Porous Carbon Materials from Zn-MOF and Its Applications

Kulandaivel Sivasankar [1,*], Souvik Pal [2,*], Murugan Thiruppathi [3] and Chia-Her Lin [2,*]

1 Department of Chemistry, Chung-Yuan Christian University, Chungli District, Taoyuan City 32023, Taiwan
2 Department of Chemistry, National Taiwan Normal University, Taipei 11677, Taiwan
3 Department of Biochemical Science and Technology, National Taiwan University, Taipei 10617, Taiwan; thiru9095@gmail.com
* Correspondence: sivasankarmpm@gmail.com (K.S.); souvikchem@ntnu.edu.tw (S.P.); chiaher@ntnu.edu.tw (C.-H.L.); Tel.: +886-2-77346221 (C.-H.L.); Fax: +886-2-29324249 (C.-H.L.)

Received: 26 November 2019; Accepted: 3 January 2020; Published: 7 January 2020

check for updates

Abstract: Nitrogen-doped porous carbon (NPC) materials were successfully synthesized via a Zn-containing metal-organic framework (Zn-MOF). The resulting NPC materials are characterized using various physicochemical techniques which indicated that the NPC materials obtained at different carbonization temperatures exhibited different properties. Pristine MOF morphology and pore size are retained after carbonization at particular temperatures (600 °C-NPC_{600} and 800 °C-NPC_{800}). NPC_{800} material shows an excellent surface area 1192 m^2/g, total pore volume 0.92 cm^3/g and displays a higher CO_2 uptake 4.71 mmol/g at 273 k and 1 bar. Furthermore, NPC_{600} material displays good electrochemical sensing towards H_2O_2. Under optimized conditions, our sensor exhibited a wide linearity range between 100 μM and 10 mM with a detection limit of 27.5 μM.

Keywords: metal-organic framework; nitrogen-doped porous carbon; carbonization; tuning pore size; CO_2 capture; H_2O_2 electrochemical sensor

1. Introduction

Porous carbon materials have been regarded as significant porous materials because of their distinctive properties such as pore size, extraordinary surface area and good electrochemical activities [1–3]. They have extensive applications in many fields including catalysis, biosensors, fuel cells and supercapacitors [4–11]. In this sense, 3D porous carbon-based structures are promising to numerous applications, such as contamination removal, gas sorption/separation, and electrode materials [2,12,13]. In particular, CO_2 capture purpose nitrogen-doped porous carbon (NPC) materials were used, because of its stability, low cost and performance [14,15]. For CO_2 capture, the pore size of porous material plays a significant role, ultramicropores of ~4 Å to ~8 Å are predominantly suitable for CO_2 sorption [16,17]. The preparation of porous carbon materials has been synthesized in a known way such as template and activation method [18,19]. Generally, template progression devours a larger quantity of organic or inorganic template and the synthesizing processes are complicated. Activation methods such as KOH and NaOH can afford a high surface area but needed a huge amount of activation agents. To avoid such complication, recently metal-organic framework (MOF) materials have gained tremendous attentions to prepare the porous carbon materials through single step carbonization method. For instance, the recently reported porous carbon material derived from Zn-MOF, having ultramicropore size (~4 Å to ~8 Å) showed excellent CO_2 capture properties [20]. Since MOFs have gained tremendous attention due to their diverse structures with tunable pore shapes, sizes, volumes, and surface chemistry. Therefore, MOFs have prospective applications in gas storage/separation, electronic devices, chemical sensors, catalysis, and biomedical applications [21–26]. The multifunctional MOFs are often chosen to synthesis porous carbon materials; MOF-templated straightforward synthesis provided the high-quality nanoporous carbon with a well-ordered pore size and significant surface area. The morphology of nanoporous carbon can be tuned by optimizing the carbonization method (such as temperature, time, and atmosphere) [1,27,28]. Recently, MOF-derived metal/metal oxide embedded porous carbon materials [29,30] are used in the electrodes for electrochemical sensors [31,32]. But, maintaining the pristine MOF morphology of the resulting porous materials from the carbonization process is a difficult task due to the shrinkage of framework/decomposing organic ligand during carbonization, therefore, a systematic study is necessary [33].

Additionally, hydrogen peroxide (H_2O_2) is a toxic oxidizing agent, being used in various fields such as biomedical science, environmental science, food, textile and chemical industries [34–36]. Therefore, H_2O_2 determination is of practical importance for both environmental and industrial purposes. It has been well established that Zn based material modified electrodes are used for H_2O_2 detection [37,38].

Therefore, herein, we reported the preparation of NPC materials from {$Zn_2(BDC)_2(DABCO)$} (Zn-MOF) [11] at various temperatures under a N_2 atmosphere (Scheme 1). The properties of the resulting NPC materials such as morphology, pore size, pore-volume, CO_2 uptake and H_2O_2 electrochemical sensing were investigated.

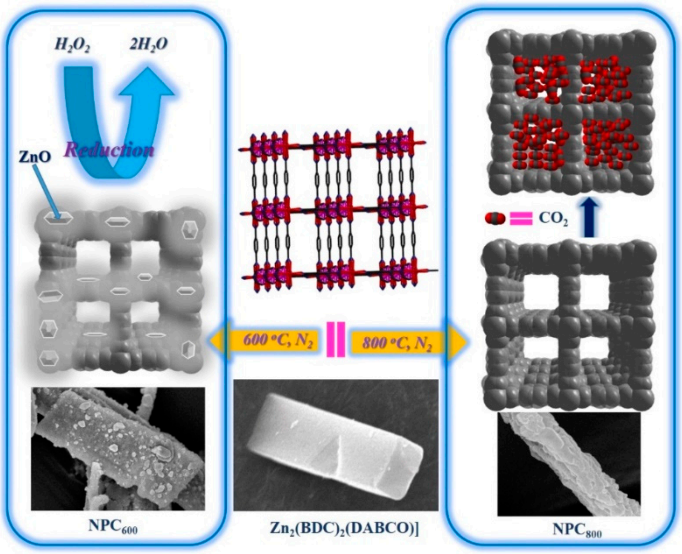

Scheme 1. Synthesizing pathway of NPC materials from Zn-MOF.

2. Methods

2.1. Materials

$Zn(NO_3)_2 \cdot 6H_2O$, (98%) and H_2BDC, (98%) were bought from Sigma-Aldrich (Burlington, MA, USA), DMF, (≥99.8%) was purchased from Merck (Darmstdt, Germany), (DABCO, 98%) was purchased from Alfa Aesar (Lancashire, UK). All other compounds used throughout this study were of an analytical grade. The electrochemical experiments were performed using a three-electrode system-CHI model 824B workstation with a screen printed carbon electrode (SPCE)/chemically modified SPCE as a working electrode, Ag/AgCl (in 3 M KCl) as a reference electrode, and Pt wire as an auxiliary electrode. SPCE was purchased from Zensor R&D (Taichung, Taiwan). A phosphate buffer solution (0.1 M, pH 7 PBS) was prepared by mixing 0.1 M, NaH_2PO_4, and Na_2HPO_4. To compare the various electrodes performance, 5 mM of FeCN solution used as a probe. Briefly, the FeCN solution was prepared using

5 mM of $K_3[Fe(CN)_6]$ and $K_4[Fe(CN)_6]$, and 0.1 M, KCl used as a supporting electrolyte. For H_2O_2 detection, 100 mM of H_2O_2 prepared from 9.8 M of H_2O_2 (30 wt%).

2.2. Preparation of Zn-MOF, {$Zn_2(BDC)_2(DABCO)$}

The Zn-MOF was prepared [39] by, a mixture of $Zn(NO_3)_2 \cdot 6H_2O$ (5.41 mmol, 1.609 g), H_2BDC (5 mmol, 0.83 g), DABCO (2.5 mmol, 0.28 g) in DMF (60 mL) was taken out into a Teflon-lined autoclave and heated to 120 °C, 2 days later cooling down to room temperature. The Zn-MOF was washed with DMF and dried at room temperature overnight. Further this material was used for the carbonization process.

2.3. Preparation of NPC Materials

The NPC materials were prepared through a single-step carbonization method [31]. The 0.400 g of Zn-MOF was transferred into a silica crucible boat and then placed in a furnace chamber. The NPC materials obtained at target temperatures (500, 550, 600, 700, 800, or 900 °C) under an N_2 atmosphere for a 5 h duration. The resulting materials obtained at 500, 550, 600, 700, 800, and 900 °C are assigned as NPC_{500}, NPC_{550}, NPC_{600}, NPC_{700}, NPC_{800} and NPC_{900} respectively.

2.4. Electrode Preparation

Prior to electrode modification, the bare SPCE was precleaned electrochemically by potential cycling between −1 and +1 V vs. Ag/AgCl for 6 cycles in 0.1 M pH 7 PBS. NPC_T modified SPCE (SPCE/NPC_T) was prepared by the following procedure: 10 µL of 2000 ppm (2 mg mL^{-1}) respective NPC_T dispersed in acetonitrile suspension was drop coated on precleaned SPCE, and allowed for dry on the hot plate at 40 °C for 15 min. The NPC_T prepared by carbonization under the increasing temperature of 500, 550, 600, 700, 800 and 900 °C. The corresponding modified electrode designated as SPCE/NPC_{500}, SPCE/NPC_{550}, SPCE/NPC_{600}, SPCE/NPC_{700}, SPCE/NPC_{800}, SPCE/NPC_{900}, respectively.

2.5. Characterization

The purity of MOF and NPC materials were investigated by powder x-ray diffraction (PXRD) using a Bruker D8 advance instrument (Billerica, MA, USA) equipped with CuKα radiation (λ = 1.54178 Å). The morphology of MOF and NPC materials were observed by high-resolution scanning electron microscopy (HR-SEM, JEOL JEM-7600F instrument, Akishima, Japan). The NPC materials morphology was characterized by transmission electron microscopy (TEM, using a JEM-2010 instrument, Tokyo, Japan) at a voltage of 200 KV. The synthesized NPC materials were also recorded with a Raman spectra on a CCD detector (Stanford Computer Optics Inc., Berkeley, CA, USA) using a He-Ne laser with an excitation wavelength of 632.8 nm. The Zn element presence was investigated by inductively coupled plasma-mass spectrometry (ICP-MS, Japan Agilent 7500ce, Tokyo, Japan). The elemental analysis (C, N, O) was executed by an elementar vario EL III CHN-OS elemental analyzer (Germany). N_2 gas adsorption, CO_2 gas adsorption of all materials were measured using micrometrics (Norcross, GA, USA) and the gas sorption analysis purpose, the materials were dried at 120 °C for 12 h under vacuum.

3. Results and Discussion

3.1. Structure, Morphology, and Composition of NPC Materials

Synthesized Zn-MOF structure and porous properties was checked by PXRD, SEM and N_2 gas sorption measurements (Figure 1a–d). As expected, the synthesized MOF showed a well-defined crystallinity and surface area of 1700 m^2/g, and good agreement with the literature [40]. The pore size of Zn-MOF was calculated by the NLDFT method, it reveals two micropores (0.75 and 1.4 nm) (Figure 1d). The SEM images revealed the particle shapes of Zn-MOF was a mixture of the cube, brick, and rod-like shapes (Figure 2c).

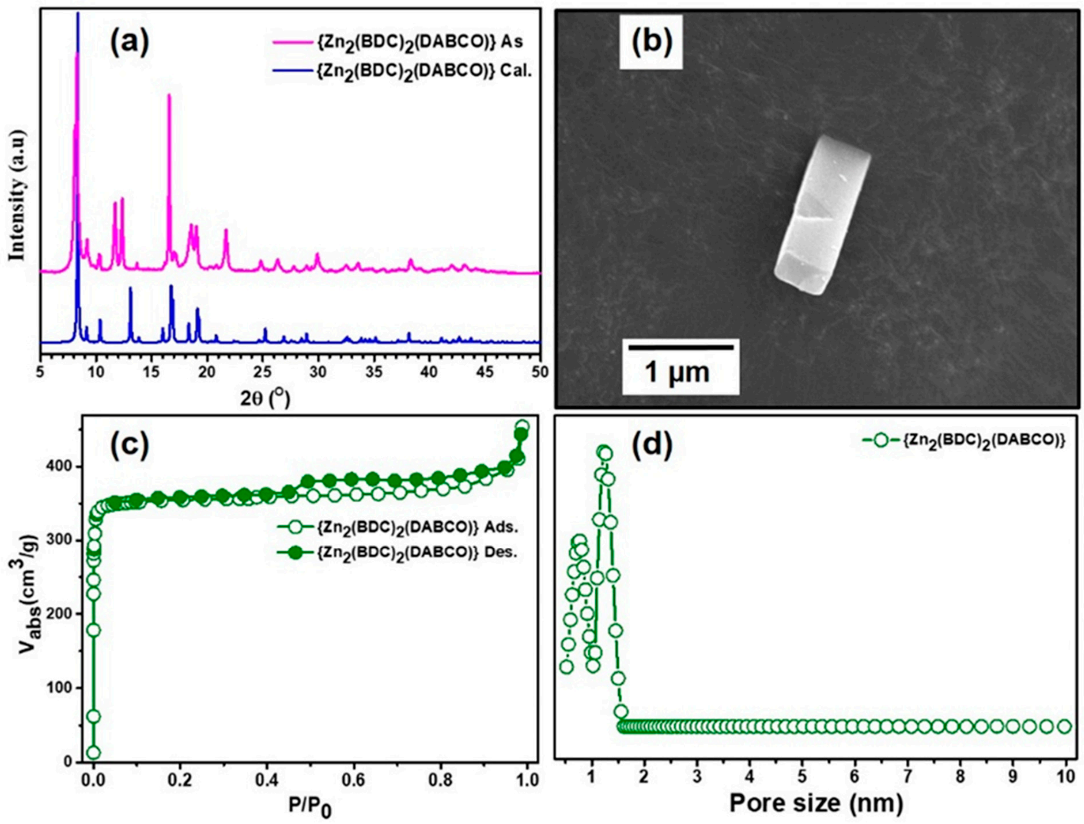

Figure 1. (**a**) PXRD patterns of as-synthesized Zn-MOF, (**b**) SEM image of Zn-MOF (**c**) N_2 sorption analysis and (**d**) NLDFT pore size distribution profile.

The MOF was further exploited to a one-step direct carbonization method to produce the NPC materials. The detailed preparation method is given in Section 2.3. The morphology, crystallinity and surface area of NPC materials were examined by PXRD, SEM, TEM, Raman analysis, N_2 gas sorption isotherms, ICP-MS, and elemental analysis.

The PXRD patterns of the $NPC_{500–700}$ samples showed the diffraction peaks for the formation of ZnO nanoparticle (Figure 2a). The 2° peaks at 31.7 (100), 34.4 (002), 36.2 (101), 47.4 (102), 56.6 (110), 62.9 (103), 65.5 (200), 68.0 (112) and 69.1 (201) that are lattice planes of ZnO [41]. The NPC_{500}, NPC_{550}, NPC_{700} morphologies show the shrinking phenomenon of Zn-MOF during carbonization at this particular temperature (Figures S1 and S2). While the morphology retained from pristine MOF, brick, and rod shape at 600 °C (Figure 2d,e and Figure S3). The PXRD pattern of the NPC_{800} sample showed two broad peaks of graphitic carbon at 23 (002) and 44° (101) (Figure 2b) [7]. The absence of ZnO at higher carbonization temperature revealed when the temperature is close to its boiling point of ZnO (907 °C) is reduced to Zn and evaporate.

Furthermore, the SEM revealed the morphology partially retained the pristine MOF with distorted graphitic carbon structures (Figure 2f,g and Figure S4), TEM images noticeably show the presence of an abundant interconnected and oriented multilayer graphene domains can be observed (Figure 3a,b). Further, by increasing the temperature to 900 °C, the PXRD pattern indicated a mixture of graphite oxide (GO) and graphitic carbon. A broad peak at 2θ ≅12 (0 0 1) the reflection of graphite oxide, 23° and 44° crystallographic planes of graphitic carbon, which possess the amorphous carbon structure. SEM (Figure 2h and Figure S5) and TEM (Figure 3c,d) images (900 °C) shown are revealed the pristine MOFs have fully or partially cracked the shapes and the shrinkage of the whole framework.

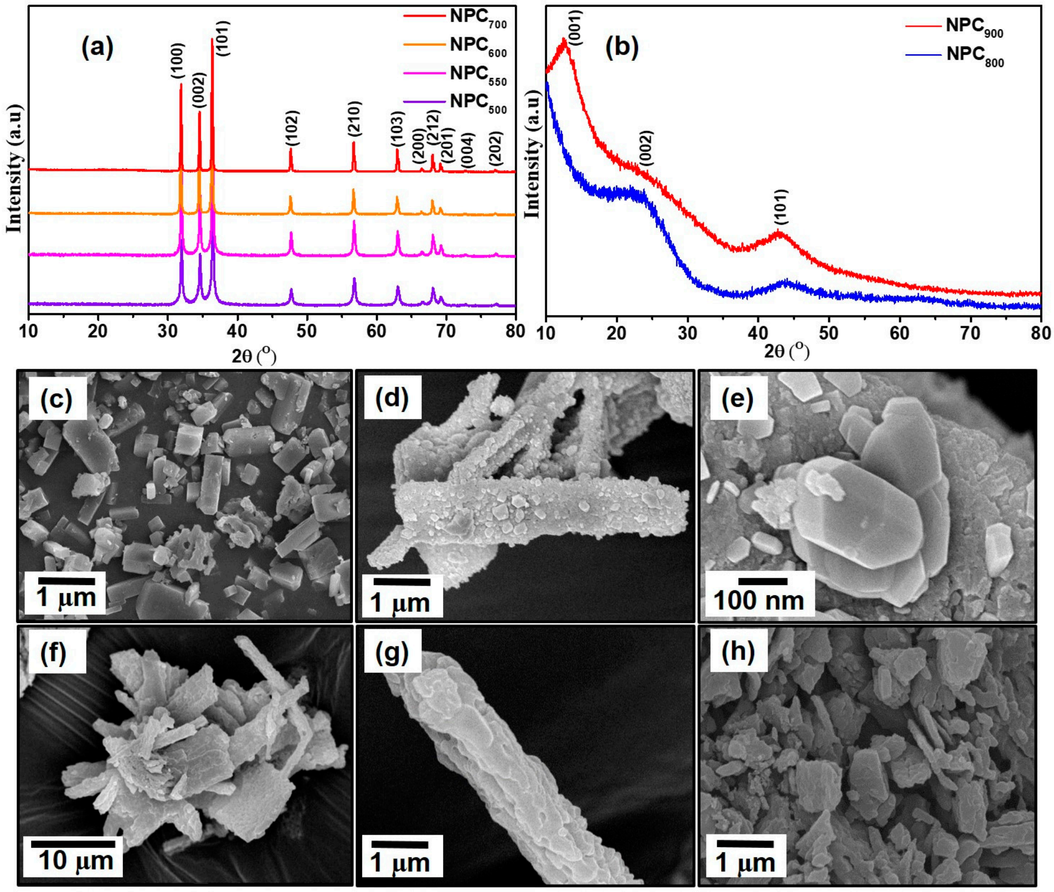

Figure 2. (**a**,**b**) PXRD patterns NPC samples. SEM images of, (**c**) synthesized Zn-MOF at the 1 µm scale (before carbonization), (**d**–**h**) Zn-MOF after carbonization at different temperature. (**d**) NPC_{600} at the 1 µm scale, (**e**) NPC_{600} at the 100 nm scale, (**f**) NPC_{800} at the 10 µm scale, (**g**) NPC_{800} at the 1 µm scale and (**h**) NPC_{900} at the 1 µm scale.

Further, synthesized NPC materials were characterized by Raman spectroscopy for the degree of graphitization. The spectrum analyzed range between 1200 cm^{-1} to 1700 cm^{-1} bands were fitted with the spectra, 1180 cm^{-1} (A_1 band), 1340 cm^{-1} (D band), and 1600 cm^{-1} (G band) [42]. Figure S6 shows significantly broadened D and G bands. Gaussian fitting was used to separate the A_1, D, G band and fitted after baseline subtraction. The I_D/I_G ratio increased while increasing the temperature, indicating the formation of disorder with a low degree of graphitization of NPC materials was obtained. The I_D/I_G ratio between D and G bands revealed the degree of graphitization in carbon-related materials. Temperature 500–700 °C carbonized materials obtained a higher degree of graphitization, due to the ZnO present in the carbon material. Because there is still a definite chemical interaction between ZnO and N atoms, the redshifts of the D bands by approximately 15 cm^{-1} to ≅1326 were observed [43]. Further, as we increased the temperature (800 and 900 °C), ZnO-N adducts were not detected and were also evidenced by PXRD. As the ratio is higher, it could be a low degree of graphitization, particularly those materials carbonized at ≥800 °C (see Table 1). The G band shifted to higher frequencies by approximately 6 cm^{-1} due to the nitrogen present in the NPC materials [44]. Chemical compositions of NPC were studied by ICP-MS and elemental analysis (Figure S7). The zinc contents were investigated by ICP-MS, increasing carbonization temperature results the decreasing zinc percentage are 51.7% (600 °C), 43.72% (700 °C), 4.95% (800 °C), 0.26% (900 °C) and an appreciable amount of nitrogen (1.96–2.98 wt%) based on elemental analysis.

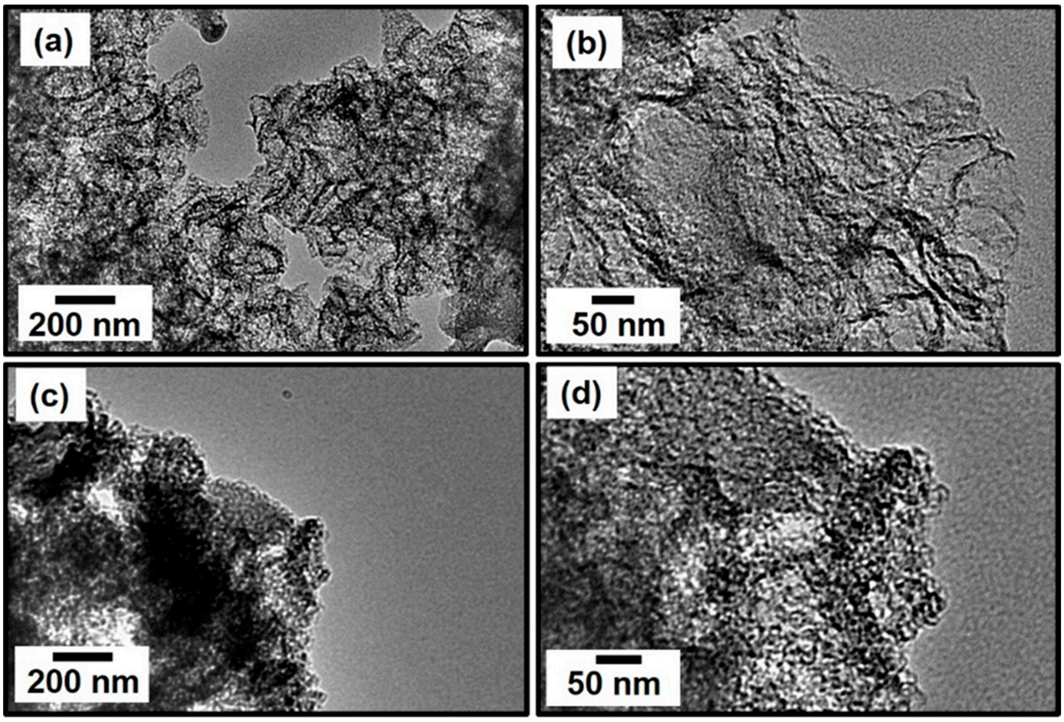

Figure 3. TEM images of (**a**) NPC_{800} at the 200 nm scale, (**b**) NPC_{800} at the 50 nm scale, (**c**) NPC_{900} at the 200 nm scale and (**d**) NPC_{900} at the 50 nm scale.

Table 1. Surface and porous properties of the NPC samples.

Sample	I_D/I_G	S_{BET} [a] (m^2/g)	V_{total} [b] (cm^3/g)	V_{micro} [c] (cm^3/g)	Pore Size (nm)	CO_2 uptake [d] (mmol/g) (wt %)
NPC_{500}	0.92	273	0.18	0.09 (50)	0.75, 1.4, 2.1~3	2.85 (12.54)
NPC_{550}	0.98	287	0.20	0.091 (45)	0.75, 1.4, 2.1~3	1.20 (5.28)
NPC_{600}	1.01	289	0.22	0.094 (42)	0.75, 1.4, 2.1~3	1.24 (5.46)
NPC_{700}	1.07	296	0.22	0.10 (45)	0.89, 1.4, 2.1~3	1.71 (7.52)
NPC_{800}	1.24	1192	0.92	0.39 (42)	0.75, 1.4, 2.1~3	4.71 (20.72)
NPC_{900}	1.25	303	0.45	0.06 (13)	1.4, 5-10	2.51 (11.04)

[a] S_{BET} surface area was examined in the P/P_0 range of 0.01 to 0.1, which gave the best linearity. [b] Total pore volume at P/P_0 = 0.99. [c] Micropore volume (≤ 2 nm) and the values in asides are the percentage of the micropore volume relative to the total pore volume (V_{micro}/V_{total}). [d] CO_2 uptake at 273 K and 1 bar and the values in asides are weight percentage (wt%).

3.2. Porous Property and CO_2 Uptake of NPC Materials

The textural properties of these NPC materials were evaluated by the N_2 sorption analyzer. The Figure 4a–c represented the N_2 uptake isotherm and corresponding pore sizes of the NPC materials. Table 1 represents the NPC material's surface area, pore volume and pore size. The N_2 sorption curves of the NPC materials possess type-I isotherms that steeply climb in the low-pressure range (P/P_0 = 0−0.10), suggesting that micropores were dominant [45]. In the high-pressure range (P/P_0 = 0.40−1.00), there were decent increases in the adsorption in all samples and a slight hysteresis loop between the sorption curves, which revealed that mesopores were also present in the materials. The surface area and total pore volume of the $NPC_{500–700}$ materials is nearly equal to 273, 287, 289, 296 m^2/g and 0.18, 0.20, 0.22, 0.22 cm^3/g correspondingly (see Table 1).

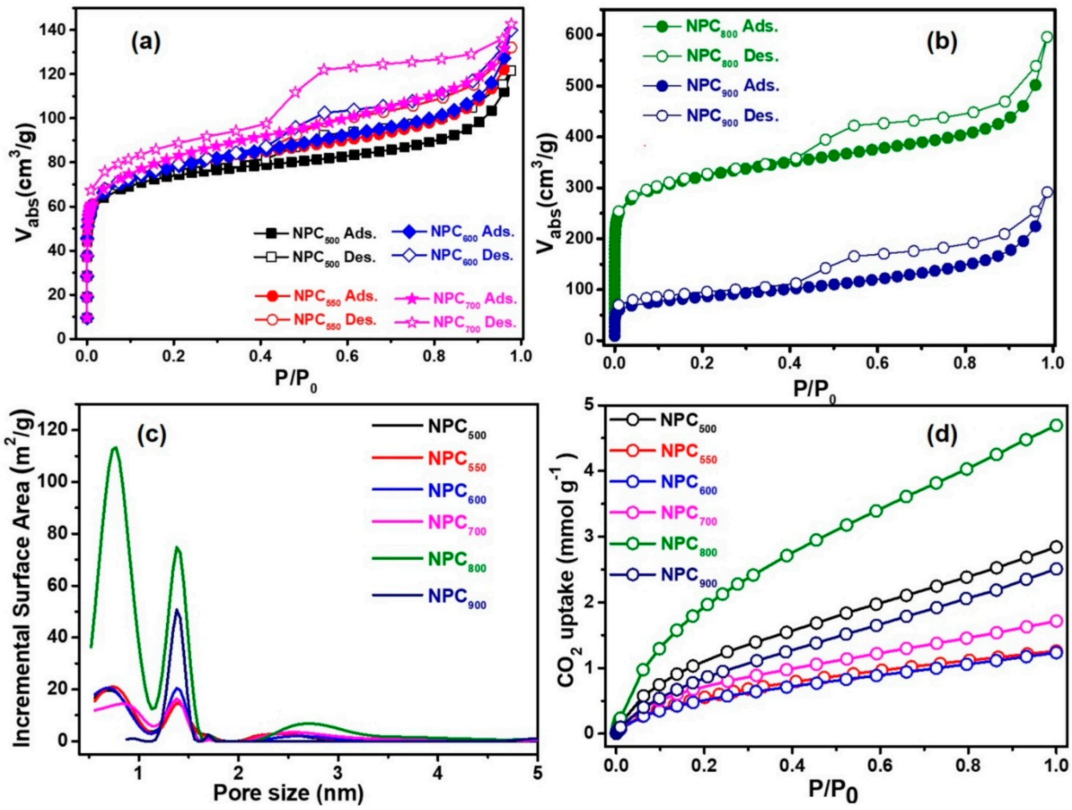

Figure 4. (**a**,**b**) N_2 sorption analysis at 77 K, (**c**) NLDFT pore size distribution profile and (**d**) CO_2 sorption isotherm at 273 K and 1 bar of NPC materials.

Whereas the BET surface area of the NPC_{800} material has 1192 m^2/g and a total pore volume 0.92 cm^3/g. The majority of the pores of $NPC_{500–800}$ materials are 0.75, 1.4 nm retained from the pristine MOF (Figure 4c), while there are mesopores around 2.1–3 nm, which specifies the occurrence of mesopores in the NPC materials (Figures S8–S13). While the NPC_{900} materials show a lesser surface area (303 m^2/g), pore volume (0.45 cm^3/g) indicates framework shrinkage and fragmentation throughout the high-temperature carbonization process. The total pore volume of NPC_{800} material has a better percentage than the $NPC_{500–700}$ and NPC_{900} materials. It is noted that the NPC_{800} material reached 42% of micropores, whereas, the percentage of V_{micro}/V_{total} decreased significantly to 13% in the NPC_{900} sample. CO_2 sorption is investigated for the NPC materials at 273 K at 1 bar (Figure 4d). NPC_{800} demonstrated a higher CO_2 capture of 4.71 mmol/g than NPC_{500} (2.85 mmol/g), NPC_{550} (1.20 mmol/g), NPC_{600} (1.24 mmol/g), NPC_{700} (1.71 mmol/g) and NPC_{900} (2.51 mmol/g) at 273 K and 1 bar. Such a micro-mesoporous structure of NPC_{800} material provides a fast diffusion of CO_2 into the inner pores material. NPC_{800} material showed CO_2 capacity value closely matches/ greater than those of the carbon-related materials (see Table S1).

3.3. Comparisons Voltammetric Behavior of Various SPCE/NPC Modified Electrode in FeCN

CV analysis was executed to study the electrochemical behavior of SPCE and SPCE/NPC_T modified electrodes in 5 mM FeCN under a potential window from –0.2 to +0.6 V. As can be seen in Figure 5, bare SPCE exhibit a well-defined reversible redox peak at E° = +193 mV with a peak to peak potential difference (ΔEp = Epa − Epc) value of 126 mV, which is the characteristic peak for Fe^{2+}/Fe^{3+} interconversion [46,47]. After SPCE/NPC_T modification, relatively higher/lower redox current responses were noticed with a ΔEp value of about 561, 235, 125, 112, 137 and 140 mV, while the relative current change (ΔIa) was recorded for SPCE/NPC_{500}, SPCE/NPC_{550}, SPCE/NPC_{600}, SPCE/NPC_{700}, SPCE/NPC_{800}, SPCE/NPC_{900} of about −99, −88, −29, −12, +83 and +113 μA, respectively.

The observation is due to the semiconductor Zn moieties existing up to a carbonization temperature of 700 °C that results in a decrease in FeCN signal. In contrary, carbonization at 800 and 900 °C produced relatively smaller Zn moieties with NPC and hence an increase in signal. This result suggests that the semiconductor Zn content decreased with increasing carbonization temperature. In other words, the FeCN current response is inversely proportional to the Zn content. The obtained results coincide with the elemental analysis, ICP-MS and PXRD results.

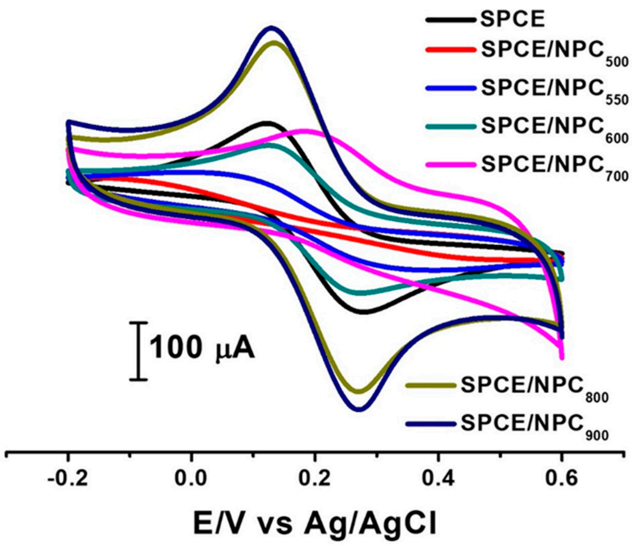

Figure 5. Cyclic voltammetric response of SPCE and SPCE/NPC_T in 5 mM ferric cyanide solution.

3.4. Detection of H_2O_2 at SPCE/NPC_T

The surface area and porous defective sites have an important role in the electrochemical sensors. Therefore, H_2O_2 sensing applicability was tested for SPCE/NPC_{500}, SPCE/NPC_{550}, SPCE/NPC_{600}, SPCE/NPC_{700}, SPCE/NPC_{800}, SPCE/NPC_{900}, respectively. Figure 6 shows electro catalytic reduction CVs of H_2O_2 at various SPCE/NPC_T electrodes. CV measurements were done in 0.1 M, pH 7.4 PB solution under the potential sweeping from 0 to −1.2 V at a scan rate of 100 mV s^{-1}. During the cathodic segment, H_2O_2 reduction peak [48] was noticed at ~−0.7 V for SPCE and for SPCE/NPC_T the same reduction peak was noticed with lower over potential (~−0.4 V). Among the various electrodes, detection response are clearer and more explicit at SPCE/NPC_{600}. These results evidently exposed that the SPCE/NPC600 electrode exhibited better electrocatalytic H_2O_2 reduction than other electrodes. Therefore, SPCE/NPC_{600} was chosen for further studies.

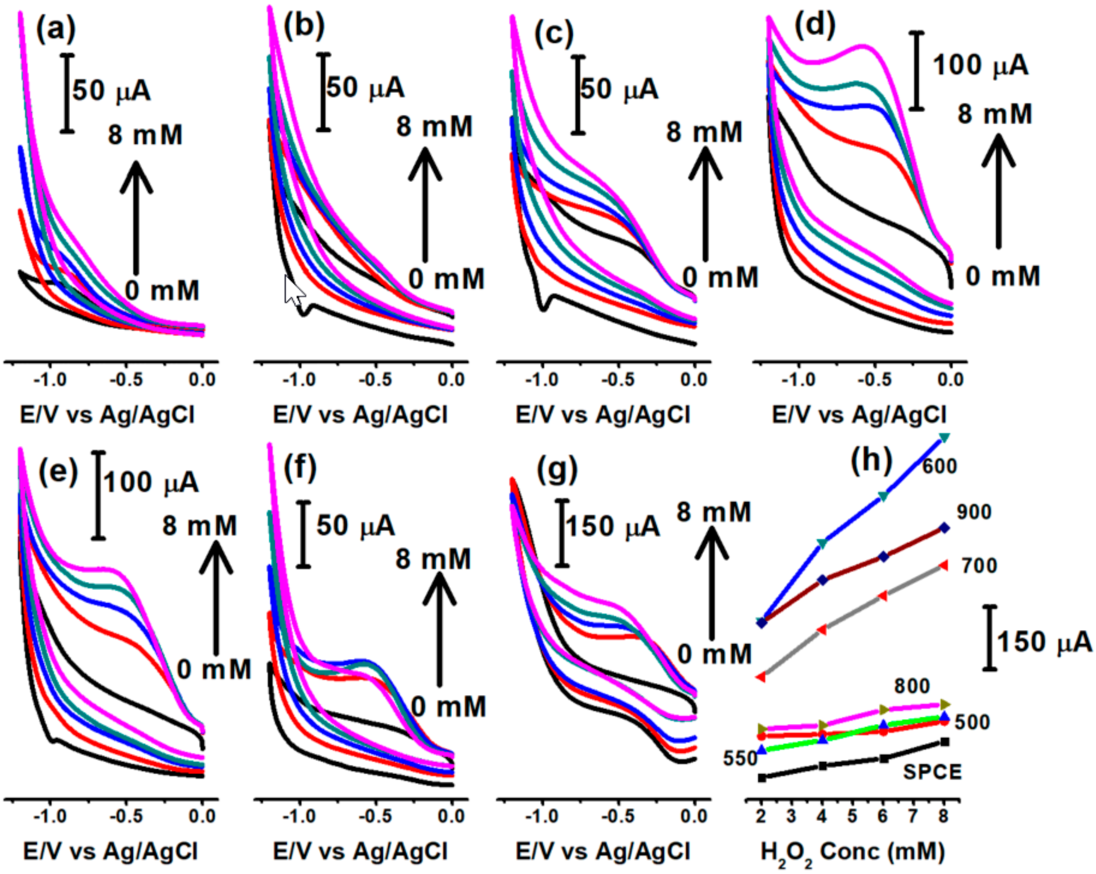

Figure 6. Cyclic voltammetric detection of H_2O_2 in 0.1 M, pH 7PB (**a**) SPCE, (**b**) SPCE/NPC_{500}, (**c**), SPCE/NPC_{550}, (**d**) SPCE/NPC_{600}, (**e**) SPCE/NPC_{700}, (**f**) SPCE/NPC_{800} and (**g**) SPCE/NPC_{900}, respectively. (**h**) Their corresponding current verses concentration plots.

3.5. Flow Injection Analysis (FIA) Detection of H_2O_2 at SPCE/NPC_{600}

The above observation was further utilized for amperometric FIA analysis of H_2O_2. The H_2O_2 reduction current increased linearly with increasing concentration, in which H_2O_2 was electrochemically reduced at −0.4 V by applying a potential, and thus yielded quantitative current responses corresponding to the content of H_2O_2 (Figure 7). A wide linearity range between 100 μM and 10 mM with a R^2 value of 0.9865 and a limit of detection (LOD) 27.5 μM were obtained. In order to access the repeatability of a SPCE/NPC_{600} modified electrode, 12 repeated injections of 0.5 mM H_2O_2 were performed and a RSD value of 4.13% was obtained. Compared to a few other Zn based H_2O_2 sensors (Table S2), the present method exhibited a wide linear range along with a specific sensitivity of 108.7 μA mM^{-1} cm^{-2}.

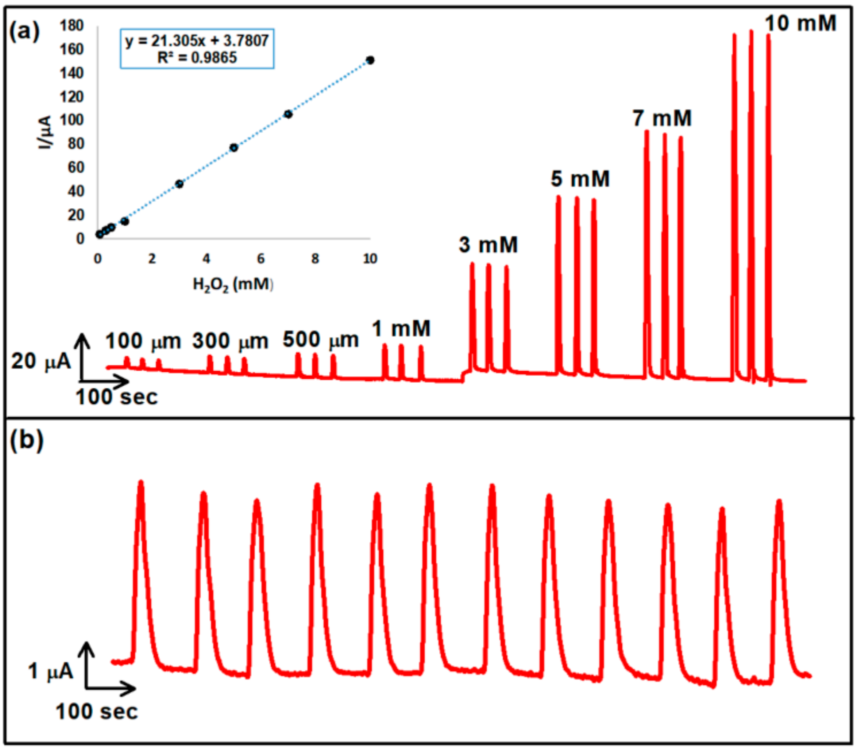

Figure 7. (**a**) Detection of H_2O_2 by FIA method at SPCE/NPC_{600}, (**b**) FIA responses of 12 continuous injections of 0.5 mM H_2O_2.

4. Conclusions

Herein, we reported the synthesized NPC materials at various carbonization temperatures at a constant time under a N_2 atmosphere. NPC materials surface, morphology, chemical composition, porous properties where characterized by PXRD, SEM, TEM, Raman spectroscopy, ICP-MS, elemental analysis, and 77 K N_2 sorption isotherms. Pristine MOF pore size was tuned to the porous carbon material, such an ultramicropore, micropore and mesopore combined in unique material and interaction between ZnO to NPC to give the pathway to synthesize the effective electrochemical property and CO_2 sorption materials. These combinations in NPC_{800} exhibited a higher CO_2 uptake of 4.71 mmol g^{-1} compare to other NPC_T materials. NPC_{600} displayed a good electrochemical reduction towards H_2O_2. Under optimal conditions, our sensor exhibited linearity that ranged from 0.1–10 mM, which confirmed its sensitive response to H_2O_2 over a wide range of concentrations. The detection limit was determined to be 27.5 µM (S/N = 3)

Supplementary Materials: The following are available online at http://www.mdpi.com/1996-1944/13/2/264/s1, Figure S1. SEM image of (a) NPC_{500} and (b) NPC_{550}. Figure S2. SEM image of NPC_{700} (a,b). Figure S3. SEM images of NPC_{600} (a–d). Figure S4. SEM image of NPC_{800} (a–d). Figure S5. SEM image of NPC_{900} (a–d). Figure S6. Raman spectra of the obtained NPC matereails. (a) NPC_{500}, (b) NPC_{550}, (c) NPC_{600}, (d) NPC_{700}, (e) NPC_{800} and (f) NPC_{900}. Figure S7. Relative atom percentage at different carbonization temperature (600–900 °C). Figure S8. NLDFT pore size distribution profile for NPC_{500}. Figure S9. NLDFT pore size distribution profile for NPC_{550}. Figure S10. NLDFT pore size distribution profile for NPC_{600}. Figure S11. NLDFT pore size distribution profile for NPC_{700}. Figure S12. NLDFT pore size distribution profile for NPC_{800}. Figure S13. NLDFT pore size distribution profile for NPC_{900}. Table S1. Comparison of CO_2 uptake with previously reported carbon related materials and MOF-derived carbon materials at temperature 273K in 1 bar. Table S2. Comparison of Zn electrode-based H_2O_2 sensors with previously reported ZnO/carbon related materials.

Author Contributions: K.S. and C.-H.L. conceived and designed the experiments; K.S. and M.T. performed the experiments, analyzed the data; K.S., M.T., and S.P. wrote the paper; C.-H.L. contributed reagents/materials/analysis tools. All authors have read and agreed to the published version of the manuscript.

Funding: Financial support received from the Ministry of Science and Technology, Taiwan (MOST107-2628-M-003-005-MY3 and MOST107-2113-M-003-017-MY2) are gratefully acknowledged.

Conflicts of Interest: The authors declare no conflicts of interest.

References

1. Jiang, H.L.; Liu, B.; Lan, Y.Q.; Kuratani, K.; Akita, T.; Shioyama, H.; Zong, F.Q.; Xu, Q. From Metal-Organic Framework to Nanoporous Carbon: Toward a Very High Surface Area and Hydrogen Uptake. *J. Am. Chem. Soc.* **2011**, *133*, 11854–11857. [CrossRef] [PubMed]
2. Yang, S.J.; Kim, T.; Im, J.H.; Kim, Y.S.; Lee, K.; Jung, H.; Park, C.R. MOF-Derived Hierarchically Porous Carbon with Exceptional Porosity and Hydrogen Storage Capacity. *Chem. Mater.* **2012**, *24*, 464–470. [CrossRef]
3. Khan, I.A.; Badshah, A.; Khan, I.; Zhao, D.; Nadeem, M.A. Soft-template carbonization approach of MOF-5 to mesoporous carbon nanospheres as excellent electrode materials for supercapacitor. *Microporous Mesoporous Mater.* **2017**, *253*, 169–176. [CrossRef]
4. Chaikittisilp, W.; Ariga, K.; Yamauchi, Y. A new family of carbon materials: Synthesis of MOF-derived nanoporous carbons and their promising applications. *J. Mater. Chem. A* **2013**, *1*, 14–19. [CrossRef]
5. Ling, P.; Hao, Q.; Lei, J.; Ju, H. Porphyrin functionalized porous carbon derived from metal–organic framework as a biomimetic catalyst for electrochemical biosensing. *J. Mater. Chem. B* **2015**, *3*, 1335–1341. [CrossRef]
6. Proietti, E.; Jaouen, F.; Lefevre, M.; Larouche, N.; Tian, J.; Herranz, J.; Dodelet, J.P. Iron-based cathode catalyst with enhanced power density in polymer electrolyte membrane fuel cells. *Nat. Commun.* **2011**, *2*, 416. [CrossRef]
7. Liu, B.; Shioyama, H.; Jiang, H.; Zhang, X.; Xu, Q. Metal-organic framework (MOF) as a template for syntheses of nanoporous carbons as electrode materials for supercapacitor. *Carbon* **2010**, *48*, 456–463. [CrossRef]
8. Khan, I.A.; Badshah, A.; Nadeem, M.A.; Haider, N.; Nadeem, M.A. A copper based metal-organic framework as single source for the synthesis of electrode materials for high-performance supercapacitors and glucose sensing applications. *Int. J. Hydrog. Energy* **2014**, *39*, 19609–19620. [CrossRef]
9. Khan, I.A.; Qian, Y.; Badshah, A.; Nadeem, M.A.; Zhao, D. Highly Porous Carbon Derived from MOF-5 as a Support of ORR Electrocatalysts for Fuel Cells. *ACS Appl. Mater. Interfaces* **2016**, *8*, 17268–17275. [CrossRef]
10. Khan, I.A.; Badshah, A.; Nadeem, M.A. Single step pyrolytic conversion of zeolitic imidazolate to CoO encapsulated N-doped carbon nanotubes as an efficient oxygen reduction electrocatalyst. *Catal. Commun.* **2017**, *99*, 10–14. [CrossRef]
11. Wang, L.; Xu, Q.; Xu, J.; Weng, J. Synthesis of hybrid nanocomposites of ZIF-8 with two-dimensional black phosphorus for photocatalysis. *RSC Adv.* **2016**, *6*, 69033–69039. [CrossRef]
12. Wei, X.; Zhang, Z.; Qin, L.; Dai, J. Template-free preparation of yeast-derived three-dimensional hierarchical porous carbon for highly efficient sulfamethazine adsorption from water. *J. Taiwan Inst. Chem. E* **2018**. [CrossRef]
13. Wei, L.; Tian, K.; Jin, Y.; Zhang, X.; Guo, X. Three-dimensional porous hollow microspheres of activated carbon for high-performance electrical double-layer capacitors. *Microporous Mesoporous Mater.* **2016**, *227*, 210–218. [CrossRef]
14. Li, Y.; Xu, R.; Wang, X.; Wang, B.; Cao, J.; Yang, J.; Wei, J. Waste wool derived nitrogen-doped hierarchical porous carbon for selective CO_2 capture. *RSC Adv.* **2018**, *8*, 19818–19826. [CrossRef]
15. Estevez, L.; Barpaga, D.; Zheng, J.; Sabale, S.; Patel, R.L.; Zhang, J.-G.; McGrail, B.P.; Motkuri, R.K. Hierarchically Porous Carbon Materials for CO_2 Capture: The Role of Pore Structure. *Ind. Eng. Chem. Res.* **2018**, *57*, 1262–1268. [CrossRef]
16. Zhang, Y.; Li, B.; Williams, K.; Gao, W.Y.; Ma, S. A new microporous carbon material synthesized via thermolysis of a porous aromatic framework embedded with an extra carbon source for low-pressure CO_2 uptake. *Chem. Commun.* **2013**, *49*, 10269–10271. [CrossRef]
17. Oschatz, M.; Antonietti, M. A search for selectivity to enable CO_2 capture with porous adsorbents. *Energy Environ. Sci.* **2018**, *11*, 57–70. [CrossRef]
18. Liu, J.; Wang, X.; Gao, J.; Zhang, Y.; Lu, Q.; Liu, M. Hollow porous carbon spheres with hierarchical nanoarchitecture for application of the high performance supercapacitors. *Electrochim. Acta* **2016**, *211*, 183–192. [CrossRef]
19. Geng, W.; Ma, F.; Wu, G.; Song, S.; Wan, J.; Ma, D. MgO-templated hierarchical porous carbon sheets derived from coal tar pitch for supercapacitors. *Electrochim. Acta* **2016**, *191*, 854–863. [CrossRef]

20. Kim, H.R.; Yoon, T.-U.; Kim, S.-I.; An, J.; Bae, Y.-S.; Lee, C.Y. Beyond pristine MOFs: Carbon dioxide capture by metal–organic frameworks (MOFs)-derived porous carbon materials. *RSC Adv.* **2017**, *7*, 1266–1270. [CrossRef]
21. He, Y.; Chen, F.; Li, B.; Qian, G.; Zhou, W.; Chen, B. Porous metal–organic frameworks for fuel storage. *Coord. Chem.* **2018**, *373*, 167–198. [CrossRef]
22. Lin, R.-B.; Xiang, S.; Xing, H.; Zhou, W.; Chen, B. Exploration of porous metal-organic frameworks for gas separation and purification. *Coord. Chem.* **2019**, *378*, 87–103. [CrossRef]
23. Du, W.; Bai, Y.-L.; Xu, J.; Zhao, H.; Zhang, L.; Li, X.; Zhang, J. Advanced metal-organic frameworks (MOFs) and their derived electrode materials for supercapacitors. *J. Power Sources* **2018**, *402*, 281–295. [CrossRef]
24. Wen, Y.; Zhang, J.; Xu, Q.; Wu, X.-T.; Zhu, Q.-L. Pore surface engineering of metal–organic frameworks for heterogeneous catalysis. *Coord. Chem.* **2018**, *376*, 248–276. [CrossRef]
25. Müller-Buschbaum, K.; Beuerle, F.; Feldmann, C. MOF based luminescence tuning and chemical/physical sensing. *Microporous Mesoporous Mater.* **2015**, *216*, 171–199. [CrossRef]
26. Nadar, S.S.; Rathod, V.K. Magnetic-metal organic framework (magnetic-MOF): A novel platform for enzyme immobilization and nanozyme applications. *Int. J. Biol. Macromol.* **2018**. [CrossRef]
27. Torad, N.L.; Hu, M.; Kamachi, Y.; Takai, K.; Imura, M.; Naito, M.; Yamauchi, Y. Facile synthesis of nanoporous carbons with controlled particle sizes by direct carbonization of monodispersed ZIF-8 crystals. *Chem. Commun.* **2013**, *49*, 2521–2523. [CrossRef]
28. Aijaz, A.; Sun, J.K.; Pachfule, P.; Uchida, T.; Xu, Q. From a metal-organic framework to hierarchical high surface-area hollow octahedral carbon cages. *Chem. Commun.* **2015**, *51*, 13945–13948. [CrossRef]
29. Chen, J.J.; Chen, Y.T.; Senthil Raja, D.; Kang, Y.H.; Tseng, P.C.; Lin, C.H. Carbonization and oxidation of metal-organic frameworks based on 1,4-naphthalene dicarboxylates. *Sci. Technol. Adv. Mater.* **2015**, *16*. [CrossRef]
30. Chen, J.J.; Chen, Y.T.; Raja, D.S.; Kang, Y.H.; Tseng, P.C.; Lin, C.H. Metal-Organic Frameworks to Metal/Metal Oxide Embedded Carbon Matrix: Synthesis, Characterization and Gas Sorption Properties. *Materials* **2015**, *8*, 5336–5347. [CrossRef]
31. Sivasankar, K.; Devasenathipathy, R.; Wang, S.-F.; Kohila rani, K.; Raja, D.S.; Lin, C.-H. Synthesis of hierarchical mesoporous graphite oxide/Al_2O_3 from MIL-100(Al) for the electrochemical determination of caffeic acid in red wine samples. *J. Taiwan Inst. Chem. E* **2018**, *84*, 188–195. [CrossRef]
32. Sivasankar, K.; Rani, K.K.; Wang, S.F.; Devasenathipathy, R.; Lin, C.H. Copper Nanoparticle and Nitrogen Doped Graphite Oxide Based Biosensor for the Sensitive Determination of Glucose. *Nanomaterials* **2018**, *8*, 429. [CrossRef] [PubMed]
33. Song, Y.; Cho, D.; Venkateswarlu, S.; Yoon, M. Systematic study on preparation of copper nanoparticle embedded porous carbon by carbonization of metal–organic framework for enzymatic glucose sensor. *RSC Adv.* **2017**, *7*, 10592–10600. [CrossRef]
34. Bai, Z.; Dong, W.; Ren, Y.; Zhang, C.; Chen, Q. Preparation of Nano Au and Pt Alloy Microspheres Decorated with Reduced Graphene Oxide for Nonenzymatic Hydrogen Peroxide Sensing. *Langmuir* **2018**, *34*, 2235–2244. [CrossRef] [PubMed]
35. Selvaraj, B.; Jen-Lin, C.; Jyh-Myng, Z. Extremely Stable Copper—Polymelamine Composite Material for Amperometric Hydrogen Peroxide Sensing. *J. Polym. Sci.* **2013**, *51*, 1639–1646. [CrossRef]
36. Qinglin, S.; Xiujuan, Q.; Jianbin, Z. The Hybrid of Gold Nanoparticles and 3D Flower-like MnO2 Nanostructure with Enhanced Activity for Detection of Hydrogen Peroxide. *Electroanalysis* **2018**, *30*, 137–145. [CrossRef]
37. Wang, J.; Xu, M.; Zhao, R.; Chen, G. A highly sensitive H_2O_2 sensor based on zinc oxide nanorod arrays film sensing interface. *Analyst* **2010**, *135*, 1992–1996. [CrossRef]
38. Al-Hardan, N.H.; Abdul Hamid, M.A.; Shamsudin, R.; Othman, N.K.; Kar Keng, L. Amperometric Non-Enzymatic Hydrogen Peroxide Sensor Based on Aligned Zinc Oxide Nanorods. *Sensors* **2016**, *16*, 1004. [CrossRef]
39. Chaemchuen, S.; Zhou, K.; Kabir, N.A.; Chen, Y.; Ke, X.; Van Tendeloo, G.; Verpoort, F. Tuning metal sites of DABCO MOF for gas purification at ambient conditions. *Microporous Mesoporous Mater.* **2015**, *201*, 277–285. [CrossRef]
40. Qadir, N.U.; Said, S.A.M.; Bahaidarah, H.M. Structural stability of metal organic frameworks in aqueous media—Controlling factors and methods to improve hydrostability and hydrothermal cyclic stability. *Microporous Mesoporous Mater.* **2015**, *201*, 61–90. [CrossRef]

41. Tarlani, A.; Fallah, M.; Lotfi, B.; Khazraei, A.; Golsanamlou, S.; Muzart, J.; Mirza-Aghayan, M. New ZnO nanostructures as non-enzymatic glucose biosensors. *Biosens. Bioelectron.* **2015**, *67*, 601–607. [CrossRef] [PubMed]
42. Gong, Y.-T.; Li, B.-H.; Pei, T.; Lin, C.-H.; Lee, S. Raman investigation on carbonization process of metal-organic frameworks. *J. Raman Spectrosc.* **2016**, *47*, 1271–1275. [CrossRef]
43. Gadipelli, S.; Guo, Z.X. Tuning of ZIF-Derived Carbon with High Activity, Nitrogen Functionality, and Yield—A Case for Superior CO_2 Capture. *ChemSusChem* **2015**, *8*, 2123–2132. [CrossRef] [PubMed]
44. Zhang, C.; Fu, L.; Liu, N.; Liu, M.; Wang, Y.; Liu, Z. Synthesis of nitrogen-doped graphene using embedded carbon and nitrogen sources. *Adv. Mater.* **2011**, *23*, 1020–1024. [CrossRef]
45. Gomez-Gualdron, D.A.; Moghadam, P.Z.; Hupp, J.T.; Farha, O.K.; Snurr, R.Q. Application of Consistency Criteria to Calculate BET Areas of Micro- and Mesoporous Metal-Organic Frameworks. *J. Am. Chem. Soc.* **2016**, *138*, 215–224. [CrossRef]
46. Thiruppathi, M.; Thiyagarajan, N.; Gopinathan, M.; Chang, J.-L.; Zen, J.-M. A dually functional 4-aminophenylboronic acid dimer for voltammetric detection of hypochlorite, glucose and fructose. *Microchim. Acta* **2017**, *184*, 4073–4080. [CrossRef]
47. Zen, J.-M.; Tsai, D.-M.; Senthil Kumar, A. Flow Injection Analysis of Ascorbic Acid in Real Samples Using a Highly Stable Chemically Modified Screen-Printed Electrode. *Electroanalysis* **2003**, *15*, 1171–1176. [CrossRef]
48. Thiruppathi, M.; Lin, P.-Y.; Chou, Y.-T.; Ho, H.-Y.; Wu, L.-C.; Ho, J.-A.A. Simple aminophenol-based electrochemical probes for non-enzymatic, dual amperometric detection of NADH and hydrogen peroxide. *Talanta* **2019**, *200*, 450–457. [CrossRef]